Interconnected Autonomous AC Microgrids via Back-to-Back Converters—Part I: Small-Signal Modeling

Mobin Naderi, *Student Member, IEEE*, Yousef Khayat, *Student Member, IEEE*, Qobad Shafiee, *Senior Member, IEEE*, Tomislav Dragicevic, *Senior Member, IEEE*, Hassan Bevrani, *Senior Member, IEEE*, and Frede Blaabjerg, *Fellow, IEEE*

***Abstract*—In this article, a set of autonomous ac microgrids, interconnected by back-to-back converters, is taken into account, where they are supplied fully using voltage source converter-based distributed energy resources. A comprehensive and generalized small-signal model of the interconnected autonomous microgrids as a large-scale system is proposed using the interconnection method. The modeling is based on detailed module models to show the impact of each module on the dynamic modes, especially the dominant critical modes. It is generalized and scalable due to separate modeling of modules as well as using unlimited and expandable interconnecting. The proposed interconnection method deals with all electrical and control connections between individual modules including feedback, feed-forward, augmentation, and the order of module inputs and outputs. The model is validated employing Prony analysis method and using output results of an OPAL-RT real-time simulator. Using the proposed modeling method, the small-signal stability analysis and controller design can be realized simply for interconnected microgrids with any number of microgrids and different structures. Typically, for two interconnected microgrids, all dynamic modes and participant state variables in different frequency ranges are identified using the eigenvalue analysis and participation matrix in MATLAB.**

***Index Terms*—Back-to-back converters, eigenvalue analysis, interconnected ac microgrids, small-signal modeling, state-space representation.**

I. Introduction

INDIVIDUAL microgrids (MGs) are independent units of modern power grids, which integrate distributed energy resources (DERs) and localize the production and consumption of electricity. Each MG consists of a group of DERs, storage systems, loads, as well as protection and control devices that can be operated in both grid-connected and autonomous modes. MGs improve the stability, reliability, economic optimality, and resiliency in comparison with individual DERs and provide auxiliary services for conventional distribution systems [1]–[3]. However, the need for improving security, reliability, sustainability, flexibility, and DER penetration level of individual MGs leads to the solution of networking [3]. If interconnected MGs (IMGs) are operated in a stable and optimal manner, they can give many advantages to local consumers and distribution systems.

IMGs can be constructed in various structures. AC/DC MGs, ac/dc interlinking lines (ILs), interlinking devices, type of interconnecting and control, as well as communication methods lead to different IMG structures [4]. Fully dc IMGs interconnected by dc ILs [5], [6], fully ac IMGs interconnected through ac ILs [7]–[12], and mixed dc and ac IMGs interconnected through dc/ac ILs and dc–ac converters [13] are presented in the literature. AC MGs are more taken into account due to their challenges in voltage and frequency controls, both active and reactive power exchanges, and the correspondence with the present ac distribution networks, which can be clustered into ac IMGs and form a new operating IMG mode.

In order to interconnect ac MGs, back-to-back converters (BTBCs), circuit breakers (CBs), and static switches can be used as interlinking devices. CBs and instantaneous static switches are used as interlinking devices in [7], [8], [10], [12], [14]–[16] that can only network ac MGs with the same nominal voltages and frequencies. In such IMGs (named by CB-IMGs), a synchronizing algorithm is required to interconnect MGs. Power exchange/sharing can be controlled by changing droop coefficients of primary controllers [7], adding a signal to secondary controllers [12], [15], or employing hierarchical control [14]. More flexible power exchange can be achieved by networking ac MGs using BTBCs [9], [11], [17]–[19]. Moreover, independent control of frequency and voltage of each MG [18], [20], power quality improvement by reactive/harmonic power interchange control [19], and integration of multiple ac MGs with different nominal voltages/frequencies [17], [18] can be addressed for IMGs via BTBCs (called BTBC-IMGs). In addition, several applications of BTBCs for bidirectional power flow between MGs and the utility grid are reported in [21] and [22].

Small-signal modeling is a well known method to understand the behavior of systems around an equilibrium point. It is engaged for autonomous MG performance and stability analysis

Manuscript received March 27, 2019; revised June 6, 2019, August 6, 2019, and September 17, 2019; accepted September 22, 2019. Date of publication September 25, 2019; date of current version February 11, 2020. Recommended for publication by Associate Editor A. Davoudi. *(Corresponding author: Mobin Naderi.)*

M. Naderi, Y. Khayat, Q. Shafiee, and H. Bevrani are with Smart/Micro Grids Research Center (SMGRC), University of Kurdistan, Sanandaj 66177-15175, Iran (e-mail: m.naderi@eng.uok.ac.ir; ykh@et.aau.dk; q.shafiee@uok.ac.ir; bevrani@uok.ac.ir).

T. Dragicevic and F. Blaabjerg are with the Department of Energy Technology, Aalborg University, 9220 Aalborg, Denmark (e-mail: tdr@et.aau.dk; fbl@et.aau.dk).

Color versions of one or more of the figures in this article are available online at http://ieeexplore.ieee.org.

Digital Object Identifier 10.1109/TPEL.2019.2943996

as well as controller design [23]–[28]. In the case of IMGs, the presented small-signal models are generally an expansion of [23]. A special configuration of MGs is considered in [9], in which any MG has a STATCOM to be coordinated with the power-exchanging BTBC. Then, an eigenvalue analysis and a robust distributed controller design are done based on the small-signal model, while BTBC modeling has not been addressed. Another modeling of BTBC-IMGs refers to multiple MGs connected to an ideal main grid, where a lower challenging structure of IMGs is concerned with respect to the grid-isolated IMGs [21]. A detailed small-signal modeling is developed for CB-IMGs and is simplified using a truncation-order reduction model [10]. Another detailed model for fully PV-based CB-IMGs is obtained in order to find oscillating modes and increase their damping [15]. An aggregation-based simplified model was presented recently, which finds a reduced-order model for CB-IMGs in low-frequency and medium-frequency dynamics [29]. More CB-IMGs are analyzed in order to define suitable range of electrical and control parameters such as interlinking line length and droop gains [10], [15], [16], [30], as well as to analyze power exchange control performance [12], [14], [31].

This article develops an easily generalized small-signal modeling method for BTBC-IMGs in the absence of a stiff main grid. Distinctive features of this article can be listed as follows.

1) Unlike all existing modeling methods for IMGs, a detailed comprehensive method is proposed, which is simply generalized for any number of MGs and interlinks by applying the interconnection method.
2) In the proposed interconnection method, each module is modeled separately by a state-space representation, then, its connections with other modules are considered in the input and output. The interconnection process will be completed without any analytical calculation and merely using valuable functions of Robust Control Toolbox (RCT) in MATLAB, which strongly decreases calculation burden/error.
3) Opposed to the existing method in [14] and [15], which needs many substitutions to obtain interconnections between modules, the proposed interconnection method is much simpler in calculation due to computing all electrical and control connections between individual modules employing RCT functions. Therefore, the overall IMG modeling is facilitated even for large ones.
4) In the proposed modeling method for IMGs, the BTBCs are included as interlinking devices, which are not taken into account in the literature [9], [10], [12], [14]–[16], [31].
5) Similar to some validation methods for power systems [32], [33], the proposed interconnection method is validated using Prony method, which compares each state variable with its waveform simulated in OPAL-RT real-time simulator.
6) Impact of the most effective state variables and corresponding parameters on the dominant modes of IMGs are recognized, which will show a remarkable effect of BTBCs on the IMG stability.

The rest of this article is organized as follows. An overview of the control structure and requirements is addressed in Section II. Section III presents a comprehensive modeling method for BTBC-IMGs, including modeling of individual MGs, ILs, BTBCs, and their interconnection. In Section IV, the proposed method is validated using Prony analysis and OPAL-RT real-time simulator. Eigenvalue analysis results are reported in Section V. Finally, the conclusion is given in Section VI.

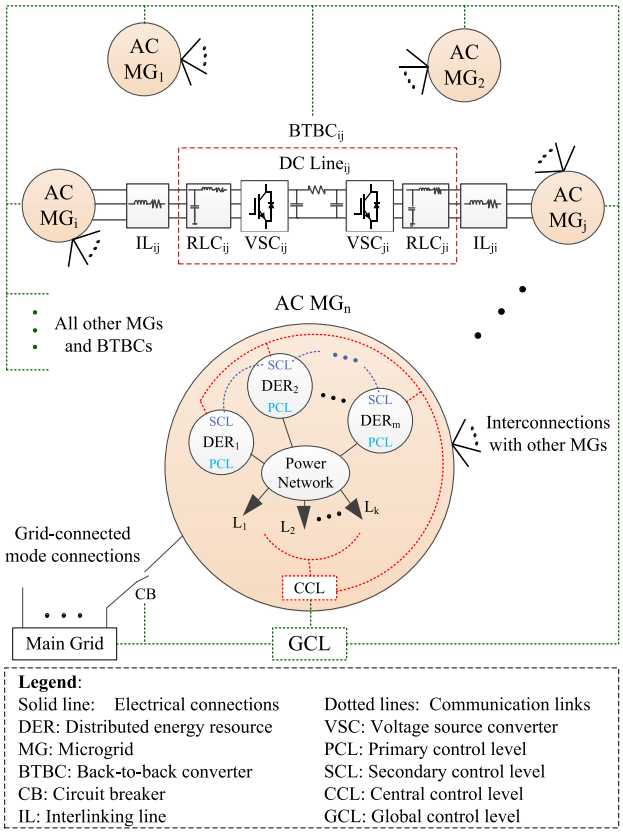

Fig. 1. AC interconnected microgrids using back-to-back converters, dc and ac interlinking lines for physical interconnection, and the four-level hierarchical control for control interconnection.

II. Control Structure and Requirements

Fig. 1 shows a general structure of ac IMGs, including autonomous MGs, ac and dc ILs, and BTBCs as the main components. The MGs may have different structures with any number of DERs, loads, and lines, which are interconnected using BTBCs, and ac/dc ILs.

The four-level hierarchical control presented in [1] is considered here to take the control responsibility of MGs in both individual and interconnected operating modes. The primary control level (PCL) comprises decentralized droop controllers implemented for each DER cascading with inner voltage and current controllers. The vital objectives of voltage/frequency stability, active/reactive power sharing, and current limiting are fulfilled in the PCL. The secondary control level (SCL) is mainly responsible for voltage/frequency restoration and power sharing improvement. However, some ancillary objectives, such as power quality improvement, may be done in the SCL. The most common architectures for the SCL are centralized and distributed types, where communication links are used to share

the data among DERs. The central control level (CCL) provides the supervisory MG capabilities, e.g., grid connecting and load shedding. The high-level energy/power management is done in the global control level (GCL). The optimal power flow among IMGs or among individual MGs and the main grid is accomplished in the GCL by communicating the production and consumption data of all participants.

In this article, the PCL is applied to each DER, which is the only active MG control loop during a small-signal disturbance. In fact, The SCL is considered to act after the primary control [28], [34], when the dynamics of the disturbance and the PCL are finished. Therefore, the SCL dynamics are not considered. Moreover, since the CCL functions, e.g., emergency control, are not of interest to be studied here, except the coordination control, they are not included. Nevertheless, the impact of SCL and CCL dynamics on the IMG stability can be studied in future works. In the IMG operating mode, the GCL role can be divided into two parts: 1) an optimization process based on the communicated data and 2) sending set points to control units including the CCLs and BTBCs as shown in Fig. 1. The first duty is outside the scope of this article, while the second one is considered to be well established. It is due to the fact that the GCL time-scale (minutes to an hour) and the CCL timescale (a few minutes) in sending set points are separated from the desired dynamics (seconds or fraction of a second). In other words, the CCL and BTBC set points sent by the GCL and the set points sent from the CCL to the downstream controllers are permanent during small-signal disturbances.

It is noteworthy to mention that the coordination among all IMGs and BTBCs is according to the GCL set points. Let us assume that a power shortage is reported to the GCL by MG_i in a specific time span. The amount of power flow to MG_i, the number of BTBCs and MGs involved, as well as MG commitment are determined by the optimal power flow management in the GCL. Hence, the GCL set points sent to all control units result in a coordinated operation for IMGs. Communicating the data in all levels is considered ideal, i.e., without dynamics.

The grid-connected mode is not considered in this article in order to focus on the stability analysis of the weak MGs interconnected by BTBCs. In addition, the IMG operating mode can be a new flexible mode, which needs to be studied in terms of stability, control, reliability, and resiliency.

III. Small-Signal Modeling of Interconnected Microgrids

A. Interconnection Method for Interconnected Microgrids

The schematic of ac IMGs in a general form is shown in Fig. 1. In order to have a comprehensive and easily generalized model of IMGs, similar modules are modeled in the same format. Then, the modeling process is divided into two main steps: 1) modeling of each module separately and 2) interconnecting all the modules using the interconnection method.

Fig. 2 shows the modeling process including both steps. The main modules consist of islanded ac MGs, ac ILs, and BTBCs. DC ILs are modeled as a part of BTBCs. Once all M modules are modeled separately in the first step, the interconnection method is applied to interconnect them in the second step. Fig. 2 is also a guideline for the interconnection method presented in Section III.

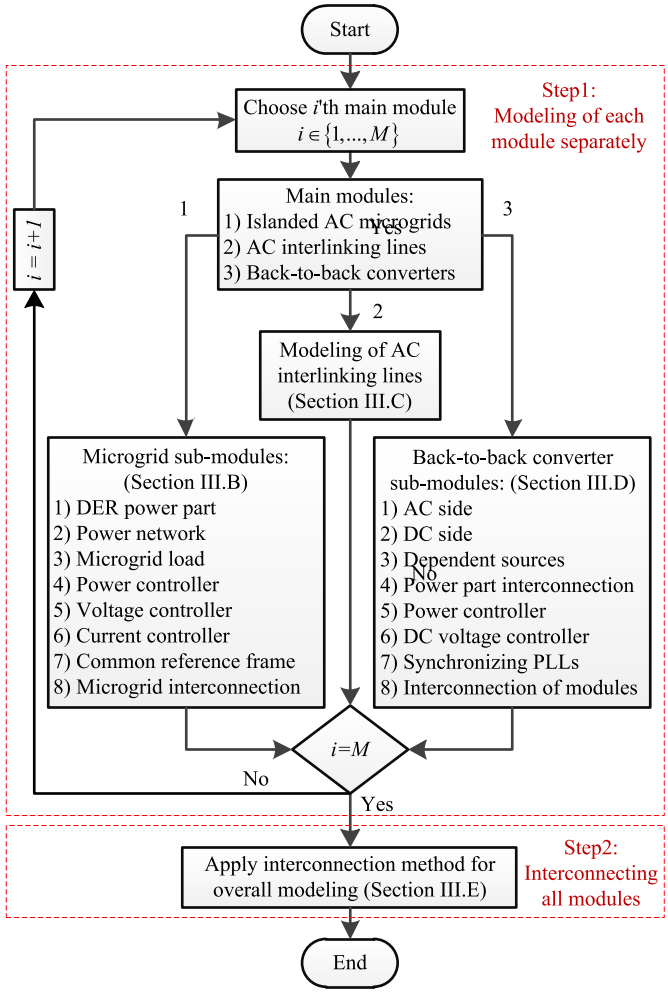

Fig. 2. Process of the proposed interconnection modeling method including two generic steps—modeling of each module separately and interconnecting all modules.

In the interconnection method, each module, i.e., an MG, a BTBC, or an ac IL is represented individually by a state-space model. The connections with other modules as shown in Fig. 1, typically for MG_i, MG_j, IL_{ij}, IL_{ji} and BTBC_{ij}, are considered in the model input/output. The interconnection process can be completed without more analytical calculation and only using RCT functions in MATLAB, which strongly reduces calculation burden/error. The RCT functions facilitate interconnecting a lot of subsystems in order to model large-scale systems, e.g., IMGs.

In the case of IMG modeling by the interconnection method.

1) Any number of separated modeled modules are transformed to system matrix form using *pck* function and are considered as subsystems using *systemnames* function;
2) All inputs to the modules are specified using *input_to* function;
3) The desired inputs and outputs for the overall model of IMGs are specified by *inputvar* and *outputvar* functions;
4) The overall model of IMGs is calculated by *sysic* function;
5) Finally, it is transformed to the state-space representation by the *unpck* function to be used in eigenvalue analysis.

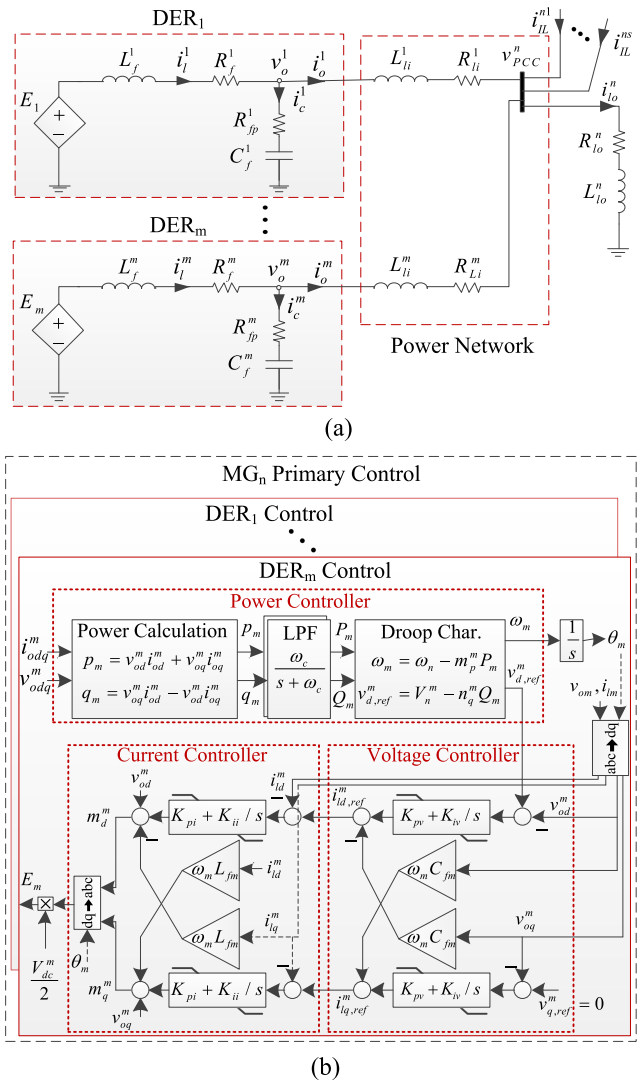

Fig. 3. Typical autonomous ac microgrid: (a) power part modules including voltage source converters, RLC filters, coupling lines, and an integrated load and (b) primary control modules including power, voltage, and current controllers.

The details of the RCT functions in the general process of interconnecting the subsystems are presented in [35].

Thus, modeling of any number of ac IMGs with different structures can be realized only by interconnecting the modules, i.e., MGs, BTBCs, and ac ILs using the proposed interconnection method. Moreover, the interconnection method is used within modeling of each main module to further facilitate overall IMG modeling.

B. Modeling of Autonomous Microgrids

In this article, a uniform structure is considered for islanded MGs due to the ease of MG formulation expression and to focus on the IMG modeling. As shown in Fig. 3(a), the structure contains the basic elements of ac MGs, including DERs, *RLC* filters, and lines. All DERs are assumed as ideal averaging modeled voltage source converters (VSCs) and a droop-based primary control is considered to share power among them as shown in Fig. 3(b).

1) DER Power Part: According to Fig. 3(a) and using circuit laws, Park transformation, and Taylor series-based linearization, the governing dynamic on the DER_m power part, including the ideal voltage source and the *RLC* filter are modeled as follows:

$$\begin{aligned}
\Delta\dot{i}^m_{ld} &= -(R_{fm}/L_{fm})\,\Delta i^m_{ld} + \omega_0 \Delta i^m_{lq} - (1/L_{fm})\,\Delta v^m_{od} \\
&\quad + (1/L_{fm})\,\Delta E^m_d + i^m_{lq0}\Delta\omega_m \\
\Delta\dot{i}^m_{lq} &= -\omega_0 \Delta i^m_{ld} - (R_{fm}/L_{fm})\,\Delta i^m_{lq} - (1/L_{fm})\,\Delta v^m_{oq} \\
&\quad + (1/L_{fm})\,\Delta E^m_q - i^m_{ld0}\Delta\omega_m \\
\Delta\dot{v}^m_{od} &= (1/C_{fm})\,i^m_{ld} + \omega_0 \Delta v^m_{oq} - (1/C_{fm})\,\Delta i^m_{od} + v^m_{oq0}\Delta\omega_m \\
\Delta\dot{v}^m_{oq} &= (1/C_{fm})\,i^m_{lq} - \omega_0 \Delta v^m_{oq} - (1/C_{fm})\,\Delta i^m_{oq} - v^m_{od0}\Delta\omega_m
\end{aligned} \tag{1}$$

where E^m_d and E^m_q are the dq-components of E_m, 0 indicates a variable value at the equilibrium point, and other parameters and variables are specified in Fig. 3. A state-space representation of (1) can be given as follows:

$$\begin{aligned}
\dot{X}^m_{DP} &= A^m_{DP}X^m_{DP} + B^m_{DP}U^m_{DP} + B^m_{PN}U^m_{PN} \\
Y^m_{DP} &= C^m_{DP}X^m_{DP} + D^m_{DP}U^m_{DP} + D^m_{PN}U^m_{PN}
\end{aligned} \tag{2}$$

where $X^m_{DP} = [\Delta i^m_{\text{ldq}} \;\; \Delta v^m_{\text{odq}}]^T$, the control input $U^m_{DP} = [\Delta E^m_{dq} \;\; \Delta\omega_m]^T$, the disturbance input $U^m_{PN} = \Delta i^m_{\text{odq}}$, $B^m_{PN} = [0_2 \;\; -(1/C^m_f)I_2]^T$, $C^m_{DP} = I_4$, $D^m_{DP} = 0_{4\times3}$, $D^m_{PN} = 0_{4\times2}$

$$A^m_{DP} = \begin{bmatrix} -R^m_f/L^m_f & \omega_0 & -1/L^m_f & 0 \\ -\omega_0 & -R^m_f/L^m_f & 0 & -1/L^m_f \\ 1/C^m_f & 0 & 0 & \omega_0 \\ 0 & 1/C^m_f & -\omega_0 & 0 \end{bmatrix}$$

$$B^m_{DP} = \begin{bmatrix} 1/L^m_f & 0 & i^m_{lq0} \\ 0 & 1/L^m_f & -i^m_{ld0} \\ 0 & 0 & v^m_{oq0} \\ 0 & 0 & -v^m_{od0} \end{bmatrix}.$$

2) Power Network: Although any type of MG power network can be considered, here, a common one, including linking lines from DERs to the point of common coupling (PCC), is assumed [see Fig. 3(a)]. The dynamic model of the mth line of the power network is expressed as follows:

$$\begin{aligned}
\Delta\dot{i}^m_{od} &= -(R^m_{li}/L^m_{li})\,\Delta i^m_{od} + \omega_0 \Delta i^m_{oq} + (1/L^m_{li})\,\Delta v^m_{od} \\
&\quad - (1/L^m_{li})\,\Delta v^m_{\text{pcc},d} + i^m_{oq0}\Delta\omega^n_{\text{com}} \\
\Delta\dot{i}^m_{oq} &= -\omega_0 \Delta i^m_{od} - (R^m_{li}/L^m_{li})\,\Delta i^m_{oq} + (1/L^m_{li})\Delta v^m_{oq} \\
&\quad - (1/L^m_{li})\,\Delta v^m_{\text{pcc},q} - i^m_{od0}\Delta\omega^n_{\text{com}}
\end{aligned} \tag{3}$$

where $\Delta\omega^n_{\text{com}}$ is the perturbed frequency form of the MG_n's common reference frame (CRF), which is explained in Section III-B7. Equation (3) is represented in a state-space form as

$$\begin{aligned}
\dot{X}^m_{PL} &= A^m_{PL}X^m_{PL} + B^m_{LD}U^m_{LD} + B^m_{LP}U^m_{LP} + B^m_{L\omega}U^m_{L\omega} \\
Y^m_{PL} &= C^m_{PL}X^m_{PL}
\end{aligned} \tag{4}$$

where $X^m_{PL} = Y^m_{PL} = \Delta i^m_{\text{odq}}, U^m_{LP} = \Delta v^m_{\text{pcc},dq}, U^m_{LD} = Y^m_{DP}$, $U^m_{L\omega} = \Delta\omega^n_{\text{com}}$, and matrices can be found using (3).

3) MG Load: In this article, an integrated series *RL* load is assumed for each MG. Hence, the relationships for the MG_n load dynamic in dq frame are similar to (3) and can be represented

as a state-space model

$$\dot{X}^n_{ML} = A^n_{ML}X^n_{ML} + B^n_{\text{MLC}}U^n_{\text{MLC}} + B^n_{\text{MLP}}U^n_{\text{MLP}}$$
$$Y^n_{ML} = C^n_{ML}X^n_{ML} \tag{5}$$

where $X^n_{ML} = Y^n_{ML} = \Delta i^n_{lo,dq}$, $U^n_{\text{MLC}} = \Delta\omega^n_{\text{com}}$, $U^n_{\text{MLP}} = \Delta v^n_{\text{pcc},dq}$, and all matrices can be easily calculated.

In the case of more loads and different power networks, (4) and (5) should be found for all lines and loads. Then, their connections can be realized by the method proposed in Section III-B8.

4) Power Controller: As shown in Fig. 3(b), the power controller of each DER consists of a power calculator, two low pass filters (LPFs), and $\omega - P$ and $V_d - Q$ droop characteristics. The droop characteristics are proportional controllers. Therefore, in order to find the small-signal model of the power controller, it is sufficient to consider the dynamics of LPFs and the integrator of the local voltage phase (θ_m) producer. According to the reason presented in Section III-B7, the angle difference of the DER$_m$'s reference frame from the CRF (δ_m) is considered as a state variable instead of the θ_m that is calculated as follows:

$$\delta_m = \theta_m - \theta^n_{\text{com}} = \int (\omega_m - \omega^n_{\text{com}})\, dt \tag{6}$$

where ω_m is the DER$_m$ frequency and θ^n_{com} is the voltage phase of the DER$_1$, which the MG$_n$'s CRF is based on. Consequently, a state-space representation is deduced as

$$\dot{X}^m_{PC} = A^m_{PC}X^m_{PC} + B^m_{PC}U^m_{PC} + B^m_{\text{com}}\Delta\omega^n_{\text{com}}$$
$$Y^m_{PC} = C^m_{PC}X^m_{PC} \tag{7}$$

where $X^m_{PC} = [\Delta\delta_m \;\; \Delta P_m \;\; \Delta Q_m]^T, U^m_{PC} = [Y^m_{DP} \;\; Y^m_{PL}]^T$, $Y^m_{PC} = [\Delta\omega_m \;\; \Delta v^m_{dq,\text{ref}} \;\; \Delta\delta_m]^T, B^m_{PC} = [B^m_{\text{PDP}} \;\; B^m_{PPL}]$, and

$$A^m_{PC} = \begin{bmatrix} 0 & -m^m_p & 0 \\ 0 & -\omega_c & 0 \\ 0 & 0 & -\omega_c \end{bmatrix} \quad B^m_{\text{PPL}} = \begin{bmatrix} 0 & 0 \\ \omega_c v^m_{od0} & \omega_c v^m_{oq0} \\ -\omega_c v^m_{oq0} & \omega_c v^m_{od0} \end{bmatrix}$$

$$B^m_{\text{PDP}} = \begin{bmatrix} 0 & 0 & 0 & 0 \\ 0 & 0 & \omega_c i^m_{od0} & \omega_c i^m_{oq0} \\ 0 & 0 & \omega_c i^m_{oq0} & -\omega_c i^m_{od0} \end{bmatrix}$$

$$C^m_{PC} = \begin{bmatrix} 0 & -m^m_p & 0 \\ 0 & 0 & -n^m_q \\ 0 & 0 & 0 \\ 1 & 0 & 0 \end{bmatrix} \quad B^m_{\text{com}} = \begin{bmatrix} -1 & 0 & 0 \end{bmatrix}^T.$$

5) Voltage Controller: Any DER in an autonomous MG has a voltage controller in order to regulate its output voltage. The d-component reference is received from the $V_d - Q$ droop characteristic and the q-component reference is set to zero. Therefore, by considering a PI controller, as shown in Fig. 3(b), and considering the output of the integrators as the state variables (X^m_{VC}), a state-space representation can be given as

$$\dot{X}^m_{VC} = A^m_{VC}X^m_{VC} + B^m_{VC}U^m_{VC}$$
$$Y^m_{VC} = C^m_{VC}X^m_{VC} + D^m_{VC}U^m_{VC} \tag{8}$$

where $U^m_{VC} = [Y^m_{DP} \;\; Y^m_{PC}]^T, Y^m_{VC} = i^{\text{ref}}_{\text{ldq}}, A^m_{CC} = 0_2, C^m_{VC} = I_2, B^m_{VC} = [B^m_{\text{VDP}} \;\; B^m_{\text{VPC}}], D^m_{VC} = [D^m_{\text{VDP}} \;\; D^m_{\text{VPC}}]$. The submatrices are $B^m_{\text{VDP}} = [0_2 \;\; -K_{iv}I_2], B^m_{\text{VPC}} = [0_{2\times1} \;\; K_{iv}I_2 \;\; 0_{2\times1}]$, and

$$D^m_{\text{VPC}} = \begin{bmatrix} 0_{1\times2} & -K_{pv} & -\omega_0 C^m_f & 0_{1\times2} \\ 0_{1\times2} & \omega_0 C^m_f & -K_{pv} & 0_{1\times2} \end{bmatrix}$$

$$D^m_{\text{VPC}} = \begin{bmatrix} -C^m_f v^m_{oq0} & K_{pv} & 0 \\ C^m_f v^m_{od0} & 0 & K_{pv} \end{bmatrix}.$$

6) Current Controller: A dq-frame PI current controller for DER$_m$ is shown in Fig. 3(b) in relation with the MG$_n$ primary control. By considering the outputs of integrators as state variables (X^m_{CC}) and applying block diagram relationships, the state-space model of the current controller is represented as

$$\dot{X}^m_{CC} = A^m_{CC}X^m_{CC} + B^m_{CC}U^m_{CC}$$
$$Y^m_{CC} = C^m_{CC}X^m_{CC} + D^m_{CC}U^m_{CC} \tag{9}$$

where $U^m_{CC} = [Y^m_{DP} \;\; Y^m_{VC} \;\; \Delta\omega_m]^T, Y^m_{CC} = m^m_{dq}, A^m_{CC} = 0_2$, $C^m_{CC} = I_2, B^m_{CC} = [B^m_{\text{CDP}} \;\; B^m_{\text{CVC}} \;\; B^m_{\text{CPC}}]$, and $D^m_{CC} = [D^m_{\text{CDP}} \;\; D^m_{\text{CVC}} \;\; D^m_{\text{CPC}}]$. The submatrices are $B^m_{\text{CDP}} = [-K_{ii}I_2 \;\; 0_2]$, $B^m_{\text{CVC}} = K_{ii}I_2, B^m_{\text{CPC}} = 0_{2\times3}, D^m_{\text{CVC}} = K_{pi}I_2, D^m_{\text{CPC}} = [-L^m_f i^m_{lq0} \;\; L^m_f i^m_{ld0}]$, and

$$D^m_{\text{CDP}} = \begin{bmatrix} -K_{pi} & -\omega_{m0}L^m_f & 1 & 0 \\ \omega_{m0}L^m_f & -K_{pi} & 0 & 1 \end{bmatrix}.$$

7) Common Reference Frame: The DER frequency references are produced independently as shown in Fig. 3(b). Though the frequencies are equal in stable steady-state operation, their dynamics can be different. Therefore, a CRF should be considered to model DER frequency interactions [10], [16], [23]. For this purpose, the following five steps are necessary.

a) One of the DER reference frames should be considered as the CRF. In this article, the reference frame of the DER$_1$ of each MG is considered as the CRF.

b) $\Delta\delta$ is determined as a state variable of each DER, which is realized in the power controller (see Section III-B4).

c) ω_{com} is used in the modeling of passive modules without self-produced frequency, such as loads and power networks.

d) The output variables of each individual reference frame to the modules, which are stated in the CRF, should be transformed to the CRF and vice versa. For instance, the $v^m_{o,dq}$ is stated in the individual mth reference frame as an input to the power network, which is stated in the CRF. Hence, $v^m_{o,dq}$ should be transformed to the CRF. Similarly, the inverse transformation is needed for i^m_{odq}. Both the transformation and its inverse in a perturbed form are as follows:

$$\Delta v_{DQ} = T_s.\Delta v_{dq} + T_{\delta 1}.\Delta\delta \tag{10a}$$
$$\Delta v_{dq} = T_s^{-1}.\Delta v_{DQ} + T_{\delta 2}.\Delta\delta \tag{10b}$$

where v_{DQ} and v_{dq} express variables in CRF and individual frames, respectively, and

$$T_s = \begin{bmatrix} \cos\delta_0 & -\sin\delta_0 \\ \sin\delta_0 & \cos\delta_0 \end{bmatrix}$$

$$T_{\delta 1} = \begin{bmatrix} -(v_{d0}\sin\delta_0 + v_{q0}\cos\delta_0) \\ v_{d0}\cos\delta_0 - v_{q0}\sin\delta_0 \end{bmatrix}$$

$$T_{\delta 2} = \begin{bmatrix} -v_{d0}\sin\delta_0 + v_{q0}\cos\delta_0 \\ -(v_{d0}\cos\delta_0 + v_{q0}\sin\delta_0) \end{bmatrix}.$$

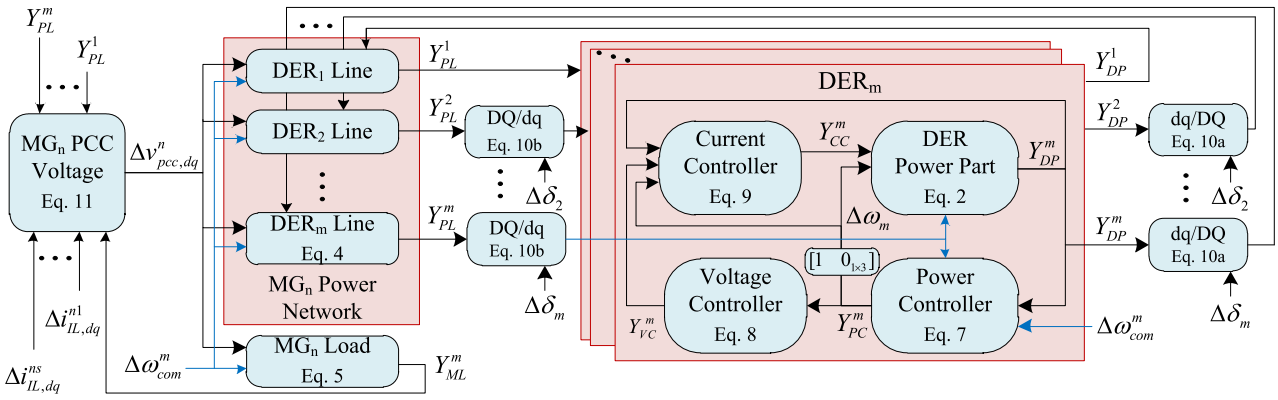

Fig. 4. All power and control interconnections of the proposed generalized modeling for *n*th autonomous ac microgrid.

e) Since the MGs are interconnected by BTBCs, where the dc links make the MG frequencies independent, individual CRFs should be considered for MGs.

8) MG Interconnection and Complete Model: In order to find an inclusive state-space representation for each MG, all partial module models presented in previous sections should be interconnected. The input and output of each module is specified and their interconnection should be based on the MG structure in each case.

According to Fig. 4, the interconnected loops of DER$_m$'s control and power parts are completely modeled by (2) and (7)–(9). On the other hand, the DER power part, the power network, and the load are correlated based on (4) and (5). $v^n_{pcc,dq}$ as a disturbance input in (4) and (5) leads to a lack of solving all differential equations independently. Therefore, a virtual resistor r_v is considered at the PCC$_n$, which results in the complementary relation to the system equations, i.e., (2), (4), (5), (7)–(9). Employing KCL at the PCC$_n$ gives

$$V^n_{\text{pcc},dq} = \sum_{k=1}^{m} R_V i^k_{\text{odq}} + \sum_{l=1}^{s} R_V i^{nl}_{IL,dq} - R_V i^n_{lo,dq} \tag{11}$$

where $R_V = r_V I_2$ and $i^{nl}_{IL,dq}$ is the current of lth IL connected to the PCC$_n$ shown in Fig. 3(a). Equation (11) should be obtained for all coupling point voltages in the case of multiple coupling points between the MG and ILs.

An intensive generalized MG model can be given according to Fig. 4, which shows the interconnections of all MG modules. Each MG with any number of DERs, lines, and loads can be represented as a state-space model

$$\begin{aligned} \dot{X}^n_{MG} &= A^n_{MG} X^n_{MG} + B^n_{MG} U^n_{MG} \\ Y^n_{MG} &= C^n_{MG} X^n_{MG} + D^n_{MG} U^n_{MG} \end{aligned} \tag{12}$$

where X^n_{MG} can be organized in any order such as

$$X^n_{MG} = [X^1_{\text{DER}} \;\; X^2_{\text{DER}} \;\dots\; \overbrace{X^m_{PD} \;\; X^m_{PC} \;\; X^m_{VC} \;\; X^m_{CC}}^{X^m_{DER}}$$

$$X^1_{PL} \;\; X^2_{PL} \;\dots\; X^m_{PL} \;\; X^n_{ML}]^T$$

and it consists of $13m + 2$ state variables for the MG structure shown in Fig. 3(a), where m is the number of DERs/lines. All IL currents to the MG$_n$ are the inputs as $U^n_{MG} = [i^{n1}_{IL,dq} \dots i^{ns}_{IL,dq}]^T$, and the impact of the MG$_n$ on the overall IMG model can be considered as $Y^n_{MG} = [\Delta\omega^n_{\text{com}} \; \Delta v^n_{\text{pcc},dq}]^T$. Finally, the matrices can be easily calculated using module models, their interconnections shown in Fig. 4, and employing the useful RCT functions in MATLAB.

C. Modeling of Interlinking Lines

The ILs are modeled as series *RL* branches as shown in Fig. 1 due to their low/medium length. The current direction is considered to be from BTBCs to MGs for all ILs. In addition, their equations are presumed to be expressed in the CRF of the connected MG. Since the dynamics are completely similar to the dynamics of the internal MG lines, (3) can be rewritten and a state-space representation for IL$_{ij}$ can be derived as

$$\begin{aligned} \dot{X}^{ij}_{IL} &= A^{ij}_{IL} X^{ij}_{IL} + B^{ij}_{\text{ILM}} U^{ij}_{\text{ILM}} + B^{ij}_{\text{ILB}} U^{ij}_{\text{ILB}} \\ Y^{ij}_{IL} &= C^{ij}_{IL} X^{ij}_{IL} \end{aligned} \tag{13}$$

where $X^{ij}_{IL} = Y^{ij}_{IL} = \Delta i^{ij}_{IL,dq}$, $U^{ij}_{\text{ILB}} = \Delta v^{ij}_{fc}$, $U^{ij}_{\text{ILM}} = [\Delta v^i_{\text{pcc},dq} \; \Delta\omega^i_{\text{com}}]^T$, and $B^{ij}_{\text{ILB}} = (1/L^{ij}_{IL}) I_2$

$$A^{ij}_{IL} = \begin{bmatrix} -\dfrac{R^{ij}_{IL}}{L^{ij}_{IL}} & \omega^i_{\text{com}0} \\ -\omega^i_{\text{com}0} & -\dfrac{R^{ij}_{IL}}{L^{ij}_{IL}} \end{bmatrix}$$

$$B^{ij}_{\text{ILM}} = \begin{bmatrix} \dfrac{-1}{L^{ij}_{IL}} & 0 & i^{ij}_{IL,q0} \\ 0 & \dfrac{-1}{L^{ij}_{IL}} & -i^{ij}_{IL,d0} \end{bmatrix}.$$

D. Back-to-Back Converter Modeling

According to Fig. 5(a), a BTBC can be controlled by two controllers in order to exchange power between two ac MGs. The power controller receives the active and reactive power references from a higher level controller, which is the GCL here, and tries to exchange scheduled powers by controlling the VSC$_i$ current. On the other hand, the dc voltage controller stabilizes the dc side voltage (V^j_{dc}) by controlling the VSC$_j$ current. In addition, two phase-locked loops (PLLs) are required for the VSCs to synchronize with the MGs. In addition, the power part

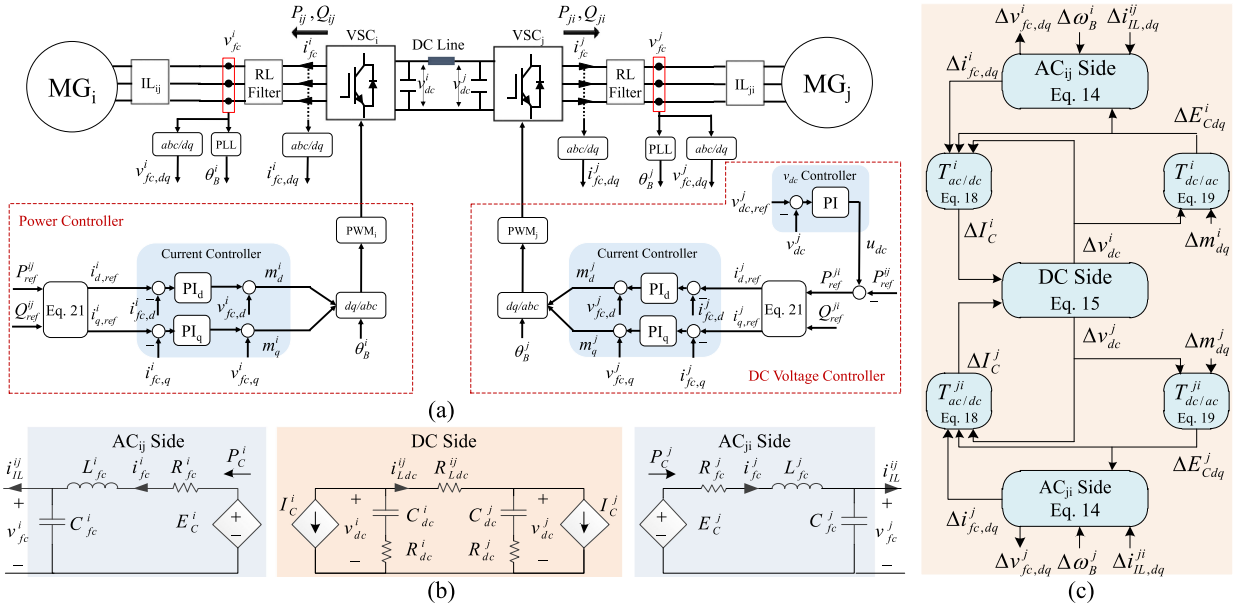

Fig. 5. Interlinking BTBC: (a) control and operation block diagram; (b) power part averaging model; and (c) power part interconnection.

comprises two ac sides and one common dc link. A precise dynamic model of a BTBC consists of ac and dc sides, power controller, dc voltage controller, and PLLs.

1) AC Side: Fig. 5(b) shows the circuit model of the BTBC power part. Each BTBC ac side is an *RLC* filter, where its dynamics are presented in (1). Hence, a similar representation to (2) can be given for the BTBC ac side as follows:

$$\dot{X}^i_{Bac} = A^i_{Bac}X^i_{Bac} + B^i_{Bac1}U^i_{Bac1} + B^i_{Bac2}U^i_{Bac2}$$
$$Y^i_{Bac} = C^i_{Bac}X^i_{Bac} \tag{14}$$

where $X^i_{Bac} = Y^i_{Bac} = [\Delta i^i_{fc,dq}\ \Delta v^i_{fc,dq}]^T, U^i_{Bac1} = [\Delta E^i_{Cdq}\ \Delta\omega^i_B]^T, U^i_{Bac2} = \Delta I^{ij}_{IL,dq}$, and the matrices are

$$A^i_{Bac} = \begin{bmatrix} -R^i_{fc}/L^i_{fc} & \omega^i_{B0} & -1/L^i_{fc} & 0 \\ -\omega^i_{B0} & -R^i_{fc}/L^i_{fc} & 0 & -1/L^i_{fc} \\ 1/C^i_{fc} & 0 & 0 & \omega^i_{B0} \\ 0 & 1/C^i_{fc} & -\omega^i_{B0} & 0 \end{bmatrix}$$

$$B^i_{Bac1} = \begin{bmatrix} \frac{1}{L^i_{fc}} & 0 & i^i_{fc,q0} \\ 0 & \frac{1}{L^i_{fc}} & -i^i_{fc,d0} \\ 0 & 0 & v^i_{fc,q0} \\ 0 & 0 & -v^i_{fc,d0} \end{bmatrix} \quad B^i_{Bac2} = \begin{bmatrix} 0_2 \\ -\left(1/C^i_{fc}\right) I_2 \end{bmatrix}.$$

2) DC Side: The currents drawn by ac sides in order to form the dependent voltage sources, i.e., E^i_C and E^j_C, are modeled by current sources I^i_C and I^j_C shown in Fig. 5(b). In addition to the VSC's capacitors and series resistors, the dc line is modeled by a resistor in the BTBC dc side. One can easily find a state-space representation as follows:

$$\dot{X}^{ij}_{Bdc} = A^{ij}_{Bdc}X^{ij}_{Bdc} + B^{ij}_{Bdc}U^{ij}_{Bdc}$$
$$Y^{ij}_{Bdc} = C^{ij}_{Bdc}X^{ij}_{Bdc} \tag{15}$$

where $X^{ij}_{Bdc} = [\Delta v^i_{dc}\ \Delta v^j_{dc}]^T, U^{ij}_{Bdc} = [\Delta I^i_C\ \Delta I^j_C]^T$, and

$$A^{ij}_{Bdc} = \begin{bmatrix} -1/\left(R^{eq}_{dc}C^i_{dc}\right) & 1/\left(R^{eq}_{dc}C^i_{dc}\right) \\ 1/(R^{eq}_{dc}C^j_{dc}) & -1/\left(R^{eq}_{dc}C^j_{dc}\right) \end{bmatrix}$$

$$B^{ij}_{Bdc} = \begin{bmatrix} \left(R^i_{dc}/R^{eq}_{dc}\right) - 1 & -\left(R^j_{dc}/R^{eq}_{dc}\right) \\ -(R^i_{dc}/R^{eq}_{dc}) & \left(R^j_{dc}/R^{eq}_{dc}\right) - 1 \end{bmatrix}$$

where $R^{eq}_{dc} = R^i_{dc} + R^j_{dc} + R^{ij}_{Ldc}$, and $C^{ij}_{Bdc} = I_2$.

3) Dependent Current and Voltage Sources: As shown in Fig. 5 (b), these sources are transformations from ac/dc side to dc/ac side, which correlate both the sides as follows:

$$I^i_C = P^i_C/v^i_{dc}$$
$$E^i_C = (1/2)m_i v^i_{dc} \tag{16}$$

where P^i_C is the produced ac power of VSC$_i$ and m_i is the pulsewidth modulation (PWM) control signal shown in Fig. 5(a). By linearizing (16), the transformations can be calculated as follows:

$$\Delta I^i_C = T^i_{ac/dc}\left[\Delta v^i_{dc}\ \Delta E^i_{Cdq}\ \Delta i^i_{fc,dq}\right]^T$$
$$\Delta E^i_{Cdq} = T^i_{dc/ac}\left[\Delta v^i_{dc}\ \Delta m^i_{dq}\right]^T \tag{17}$$

where

$$T^i_{ac/dc} = \frac{3}{2v^i_{dc0}}\left[-\frac{2}{3}I^i_{C0}\ E^i_{Cd0}\ E^i_{Cq0}\ i^i_{fc,d0}\ i^i_{fc,q0}\right] \tag{18}$$

$$T^i_{dc/ac} = \frac{1}{2}\begin{bmatrix} m^i_{d0} & v^i_{dc0} & 0 \\ m^i_{q0} & 0 & v^i_{dc0} \end{bmatrix}. \tag{19}$$

4) BTBC Power Part Interconnection: In order to simplify the BTBC modeling, the power part interconnections among ac and dc sides and independent voltage and current sources are fulfilled before the control modeling. Fig. 5(c) displays this interconnection, which consists of the BTBC power modules and their interconnections with each other and the outside.

The state-space representation is calculated readily using the interconnection method, which can be expressed as

$$\dot{X}_{BP}^{ij} = A_{BP}^{ij} X_{BP}^{ij} + B_{BP}^{ij} U_{BP}^{ij}$$
$$Y_{BP}^{ij} = C_{BP}^{ij} X_{BP}^{ij} + D_{BP}^{ij} U_{BP}^{ij} \quad (20)$$

where X_{BP}^{ij} is a 10×1 vector, including the state variables of the ac and dc sides as $X_{BP}^{ij} = [X_{B\text{ac}}^{i}\ X_{B\text{ac}}^{j}\ X_{B\text{dc}}^{ij}]$ and

$$U_{BP}^{ij} = \left[\Delta m_{dq}^{i}\ \Delta\omega_{B}^{i}\ \Delta m_{dq}^{j}\ \Delta\omega_{B}^{j}\ \Delta i_{IL,dq}^{ij} \Delta i_{IL,dq}^{ji}\right]^{T}$$
$$Y_{BP}^{ij} = \left[\Delta i_{fc,dq}^{i}\ \Delta i_{fc,dq}^{j}\ \Delta v_{\text{dc}}^{j}\ \Delta v_{fc,dq}^{i}\ \Delta v_{fc,dq}^{j}\right]^{T}.$$

The matrices A_{BP}^{ij}, B_{BP}^{ij}, C_{BP}^{ij}, and D_{BP}^{ij} are calculated numerically for an input data using the RCT functions.

5) Power Controller: Here, a current control method is employed to control the BTBC power exchange. In this method, the power references P_{ref}^{ij} and Q_{ref}^{ij} are provided by the GCL. Then, the current references $i_{dq,\text{ref}}^{ij}$ are calculated as follows [36]:

$$i_{d,\text{ref}}^{ij} = 2P_{\text{ref}}^{ij}/3v_{fc,d}^{i}$$
$$i_{q,\text{ref}}^{ij} = 2Q_{\text{ref}}^{ij}/3v_{fc,d}^{i}. \quad (21)$$

It is easy to obtain a state-space model similar to the PI current controller model of DERs, i.e., (9), by considering the integrator outputs of the PI controllers as the state variables (X_{Bpc}^{i}) as follows:

$$\dot{X}_{Bpc}^{i} = A_{Bpc}^{i} X_{Bpc}^{i} + B_{Bpc}^{i} U_{Bpc}^{i}$$
$$Y_{Bpc}^{i} = C_{Bpc}^{i} X_{Bpc}^{i} + D_{Bpc}^{i} U_{Bpc}^{i} \quad (22)$$

where $U_{Bpc}^{i} = [\Delta V_{PCC,dq}^{i}\ \Delta i_{fc,dq}^{i}\ \Delta i_{dq,\text{ref}}^{i}\ \Delta\omega_{B}^{i}]^{T}$, $Y_{Bpc}^{i} = \Delta m_{dq}^{i}$, the matrices are $A_{Bpc}^{i} = 0_2$, $B_{Bpc}^{i} = [B_{Bpc1}^{i}\ B_{Bpc2}^{i}\ B_{Bpc3}^{i}\ B_{Bpc4}^{i}]$, $C_{Bpc}^{i} = (2/V_{\text{dc}})I_2$, $D_{Bpc}^{i} = [D_{Bpc1}^{i}\ D_{Bpc2}^{i}\ D_{Bpc3}^{i}\ D_{Bpc4}^{i}]$, and the submatrices are $B_{Bpc1}^{i} = 0_2$, $B_{Bpc2}^{i} = -K_{Bi}^{i} I_2$, $B_{Bpc3}^{i} = K_{Bi}^{i} I_2$, $B_{Bpc4}^{i} = 0_{2\times 1}$, $D_{Bpc1}^{i} = (2/V_{\text{dc}})I_2$, $D_{Bpc3}^{i} = (2K_{Bp}^{i}/V_{\text{dc}})I_2$, and

$$D_{Bpc2}^{i} = \frac{2}{V_{\text{dc}}}\begin{bmatrix} -K_{Bp}^{i} & -L_{fc}^{i}\omega_{B}^{i} \\ L_{fc}^{i}\omega_{B}^{i} & -K_{Bp}^{i} \end{bmatrix}$$
$$D_{Bpc4}^{i} = \frac{2}{V_{\text{dc}}}\begin{bmatrix} -L_{fc}^{i} i_{fc,q0}^{i} \\ L_{fc}^{i} i_{fc,d0}^{i} \end{bmatrix}.$$

K_{Bp}^{i} and K_{Bi}^{i} are the proportional and integral gains of the PI current controller and V_{dc} is the nominal dc link voltage.

6) DC Voltage Controller: In order to have a stable BTBC operation, the VSC$_j$ needs to exchange the same active power with the VSC$_i$ by applying $-P_{\text{ref}}^{ij}$ as the active power reference. In addition, the dc voltage should be controlled through the same control signal. On the other hand, although the VSC$_j$'s reactive power reference is free from the VSC$_i$'s Q_{ref}^{ij}, usually references with equal magnitudes are of interest. Therefore, power references of the VSC$_j$ are expressed as

$$P_{\text{ref}}^{ji} = u_{\text{dc}} - P_{\text{ref}}^{ij} Q_{\text{ref}}^{ji} = -Q_{\text{ref}}^{ij} \quad (23)$$

where u_{dc} is the control effort of the V_{dc}^{j} controller shown in Fig. 5(a). Thus, the current references can be calculated by (21)

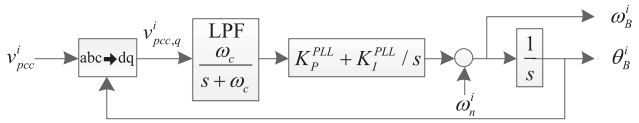

Fig. 6. Structure of PLL typically used for VSC$_i$.

and a state space can be represented for VSC$_j$ current controller similar to (22) as follows:

$$\dot{X}_{Bvc}^{j} = A_{Bvc}^{j} X_{Bvc}^{j} + B_{Bvc}^{j} U_{Bvc}^{j}$$
$$Y_{Bvc}^{j} = C_{Bvc}^{j} X_{Bvc}^{j} + D_{Bvc}^{j} U_{Bvc}^{j} \quad (24)$$

where X_{Bvc}^{j} is a 2×1 vector of the integrator outputs of the PI controllers. Since the current controller structure is the same for the power controller and the dc voltage controller, the input vector, output vector, and all matrices and submatrices are equal to those of the BTBC power controller expressed following (22) with superscript j.

The V_{dc}^{j} controller, which is usually a PI controller, is modeled using state-space representation as follows:

$$\dot{X}_{\text{DVC}}^{j} = B_{\text{DVC}}^{j} U_{\text{DVC}}^{j}$$
$$Y_{\text{DVC}}^{j} = C_{\text{DVC}}^{j} X_{\text{DVC}}^{j} + D_{\text{DVC}}^{j} U_{\text{DVC}}^{j} \quad (25)$$

where X_{DVC}^{j} is the integrator output, $U_{\text{DVC}}^{j} = \Delta v_{\text{dc}}^{j}, Y_{\text{DVC}}^{j} = \Delta i_{d,ref}^{j}, B_{\text{DVC}}^{j} = K_{i}^{\text{DVC}}, C_{\text{DVC}}^{j} = [2/3v_{fc,d}^{i}\ 0]^{T}$, and $D_{\text{DVC}}^{j} = [2K_{p}^{\text{DVC}}/3v_{fc,d}^{i}\ 0]^{T}$. K_{p}^{DVC} and K_{i}^{DVC} are the proportional and integral gains of the V_{dc}^{j} PI controller.

7) Synchronizing PLLs: As mentioned earlier, the BTBC needs two PLLs to synchronize ac sides with the MG's PCC voltages through ILs. The typical PLL structure is indicated in Fig. 6. An LPF is used to clear the $v_{\text{pcc},q}^{i}$ signal and a PI controller is used to enforce it to zero in order to lock θ_{B}^{i} on the phase of v_{pcc}^{i}. Before enabling the BTBC to exchange the power, $v_{fc}^{i} = v_{\text{pcc}}^{i}$. Therefore, v_{pcc}^{i} is measured by the v_{fc}^{i} transducer. In order to find the small-signal model of the PLL, PI and LPF integrator outputs are considered as state variables. The third state variable is $\delta_{B}^{i} = \theta_{B}^{i} - \theta_{\text{com}}^{i}$ to state all BTBC ac side dynamics into the related CRF, e.g., VSC$_i$ dynamics state into the MG$_i$ CRF. Therefore, the state-space representation is as follows:

$$\dot{X}_{\text{PLL}}^{i} = A_{\text{PLL}}^{i} X_{\text{PLL}}^{i} + B_{\text{PLL}}^{i} U_{\text{PLL}}^{i}$$
$$Y_{\text{PLL}}^{i} = C_{\text{PLL}}^{i} X_{\text{PLL}}^{i} \quad (26)$$

where $U_{\text{PLL}}^{i} = [\Delta v_{\text{pcc},q}^{i}\ \Delta\omega_{\text{com}}^{i}]^{T}, Y_{\text{PLL}}^{i} = [\Delta\omega_{B}^{i}\ \Delta\delta_{B}^{i}]$, and

$$B_{\text{PLL}}^{i} = \begin{bmatrix} 0 & \omega_c & 0 \\ 0 & 0 & -1 \end{bmatrix}^{T} \quad C_{\text{PLL}}^{i} = \begin{bmatrix} 1 & K_{P}^{\text{PLL}} & 0 \\ 0 & 0 & 1 \end{bmatrix}$$
$$A_{\text{PLL}}^{i} = \begin{bmatrix} 0 & K_{I}^{\text{PLL}} & 0 \\ 0 & -\omega_c & 0 \\ 1 & K_{P}^{\text{PLL}} & 0 \end{bmatrix}.$$

8) Complete Interconnection of BTBC Modules: As the final step, the interconnections among all power and control modules represented by (20), (22), and (24)–(26) should be considered

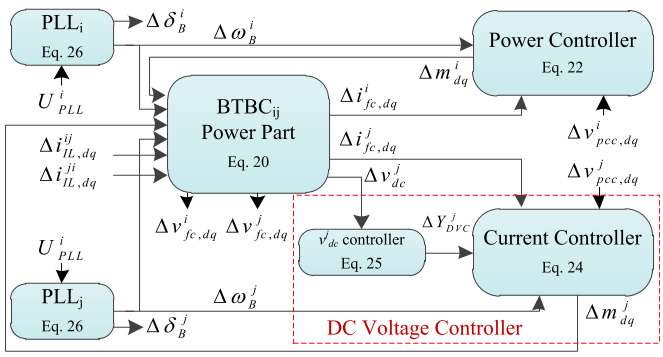

Fig. 7. Interconnections of power and control modules of the BTBC$_{ij}$.

as shown in Fig. 7. The BTBC$_{ij}$ is modeled as

$$\dot{X}_B^{ij} = A_B^{ij} X_B^{ij} + B_B^{ij} U_B^{ij}$$
$$Y_B^{ij} = C_B^{ij} X_B^{ij} + D_B^{ij} U_B^{ij} \tag{27}$$

where X_B^{ij} is a 21×1 state vector as

$$X_B^{ij} = \left[X_{BP}^{ij}\ X_{Bpc}^{i}\ X_{Bcc}^{j}\ X_{\text{DVC}}^{j}\ X_{\text{PLL}}^{i}\ X_{\text{PLL}}^{j}\right]^T.$$

By specifying the input and output vectors as $U_B^{ij} = [\Delta v_{\text{pcc},dq}^i\ \Delta i_{IL,dq}^{ij}\ \Delta v_{\text{pcc},dq}^j\ \Delta i_{IL,dq}^{ji}\ \Delta\omega_{\text{com}}^i\ \Delta\omega_{\text{com}}^j]^T$ and $Y_B^{ij} = [\Delta v_{fc,dq}^i\ \Delta v_{fc,dq}^j\ \Delta v_{\text{dc}}^j\ \Delta\delta_B^i\ \Delta\delta_B^j]^T$, considering the interconnections shown in Fig. 7 among all the BTBC modules, and using RCT functions in the interconnection method, the matrices can be calculated numerically for certain input data.

E. Overall Interconnection of Interconnected Microgrids

By modeling all ac IMG modules, including ac MGs, BTBCs, and ac/dc ILs, modeling of various structures of IMGs with any number of MGs and interconnections is possible using the interconnection method. Fig. 8 indicates the IMG interconnection focusing on the interconnection between MG$_i$ and MG$_j$ including BTBC$_{ij}$, IL$_{ij}$, IL$_{ji}$, and all modeling requirements (see Fig. 1). In fact, MG$_i$, $i = 1, \ldots, n$ can be interlinked to all other MGs, e.g., MG$_j$, $j = 1, \ldots, n$ and $j \neq i$ through the corresponding BTBCs and ILs, which shows the generality of the interconnection method.

The MGs have independent CRFs, where their functional zones are shown in Fig. 8. All ILs and BTBC ac sides connected to each MG are covered by its CRF. Therefore, (10a) and (10b) are used for power interconnections between the MG/IL with the BTBC. The small-signal model can be represented in a free motion state-space form as

$$\dot{X}_{\text{IMG}} = A_{\text{IMG}} X_{\text{IMG}} \tag{28}$$

where X_{IMG} consists of the state variables of all participating modules in the IMGs and can be expressed as

$$X_{\text{IMG}} = [\overbrace{X_{MG}^1\ \ldots\ X_{MG}^n}^{MGs}\ \overbrace{\ldots\ X_{IL}^{ij}\ \ldots}^{\text{ILs}}\ \overbrace{\ldots\ X_B^{ij}\ \ldots}^{BTBCs}]^T$$

including $(13m + 2)n + 2p + 21q$ state variables, where n, p, and q are the number of MGs, ILs, and BTBCs, respectively. A_{IMG} can be expressed in a general form as

$$A_{\text{IMG}} = [A_{rs}], r, s = 1, \ldots, t \tag{29}$$

where p is the number of all IMG modules and $A_{rs} = \mathbf{0}$ when $r \neq s$ and there is no direct connection between the rth and sth modules, otherwise $A_{rs} \neq \mathbf{0}$. $\mathbf{0}$ is a zero matrix with the appropriate size.

For each IMG case with certain data, A_{IMG} can be calculated numerically by considering the module connections as generally shown in Fig. 8, and applying the interconnection method.

F. Comparison With the Substitution Modeling Method

If the substituting method is employed for finding the complete MG model, the number of substitutions can be found according to Fig. 4 and the output arrows from the equations blocks. By the left, (11) should be substituted in (4) for all m lines and in (5) for the load, which are totally $m + 1$ substitutions. Equation (5) should be substituted in (11), and (4) should be replaced in (10b) for all m lines without the coupling DER$_1$ line (m substitution). Equation (10b) is replaced in (2) and (7) for all DERs except DER$_1$, in which the replacement is from (5) ($2m$ substitutions). By substituting (2) in (7), (9), and (10a), (9) in (2), (8) in (9), and finally changed-dimension output of (7) in (2), (9), and (8), $7m$ substitutions are required for all DERs. The substitution process can be completed by replacing (10a) in (4) for all m lines except DER$_1$ line, in which the substitution is from (2) to (4) (m substitutions). All required manual substitutions are $12m + 1$ that can be expressed as 13 when similar substitutions are just considered as one substitution, i.e., $m = 1$.

A similar substituting process is needed for BTBCs using Figs. 5(c) and 7 that leads to 24 substitutions. Neglecting similar substitutions, required that ones are reduced to 13.

According to Fig. 8, for each interconnection between two MGs, 20 substitutions (ten by neglecting the similar ones) are required. For n different autonomous ac MGs with k interconnections/BTBCs as shown in Fig. 8, totally $\sum_{i=1}^{n}(12m_i + 1) + 44k$ substitutions (36 by neglecting the similar ones) are necessary to find the IMG model using the substitution method. Such a manual calculation process leads to a high calculation burden and may be accompanied by some errors. However, in the proposed interconnection method, the large number of substitutions are fulfilled numerically using the RCT functions with a low manual calculation burden only for specifying inputs of each module employing the preprovided interconnections by Figs. 4, 5(c), 7, and 8. In fact, the calculation time/burden of the interconnection method can be determined as specifying the inputs of modules using *input_to* function with respect to substituting the equations into each other in the substitution method. The number of specifying input vectors as a relatively time-consuming process is equal to the number of modules to be interconnected. Therefore, one can easily calculate it regarding Figs. 4, 5(c), 7, and 8 as $\sum_{i=1}^{n}(7m_i + 2) + 20k$.

Both substitution and interconnection modeling methods lead to the same results (e.g., from eigenvalue analysis or time-domain simulation), since both are based on the same module models and the same strategy for selecting the input, output, and state variables. The difference is only in the calculation burden and possible calculation errors.

Table I shows the calculation burden/error comparison for the common substitution method [14], [15] and the proposed interconnection method in two sample IMGs. In this comparison

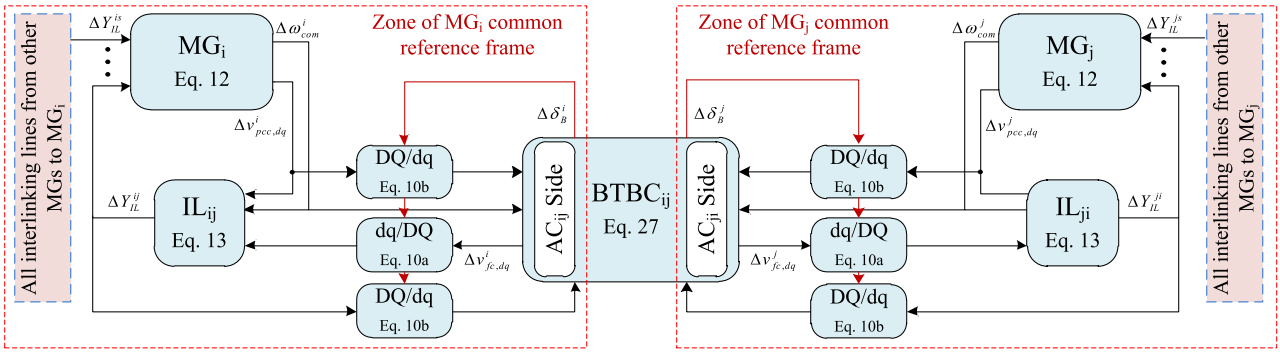

Fig. 8. Complete interconnection of ac microgrids focusing on the connection between MG_i and MG_j through IL_{ij}, IL_{ji}, and $BTBC_{ij}$.

TABLE I
COMPARISON OF THE COMMON SUBSTITUTION [14], [15] AND PROPOSED INTERCONNECTION METHODS

Modeling method	Possible manual error	Studied system	Number of substitution /*input_to*	Manual calculation time (min)
Substitution	Module modeling and substituting	IMG_1	291	1164
		IMG_2	676	2704
Interconnection	Module modeling and input specifying	IMG_1	157	157
		IMG_2	366	366

study, IMG_1 is formed by three interconnected MGs through three BTBCs, where MG_1 has three DERs, MG_2 has four DERs, and MG_3 has six DERs. IMG_2 is composed of eight interconnected MGs through seven BTBCs, where each one of MG_1-MG_3 has two DERs, each one of MG_4-MG_6 has three DERs, and MG_7 and MG_8 consist of five and ten DERs, respectively. It is obvious that the number of substitutions are larger than the number of specifying inputs in each case. Moreover, one can consider approximate average calculation times for specifying inputs as a fast manual process and substituting equations as a slow manual process as 30 s and 4 min, respectively. Hence, as shown in Table I, the total calculation time of the substitution method for the same case studies is much more than the corresponding time of the interconnection method. In addition, substituting equations may lead to different nested forms, which causes long calculation times or even manual calculation errors. However, specifying inputs is a straightforward MATLAB coding process without arithmetic complications.

IV. MODELING VALIDATION

Prony method is used for validating the power system model in [32]. For this purpose, the small-signal model of the IMG is analyzed using eigenvalue analysis and participation matrix. Thus, the participating eigenvalues and their contribution amount in each state variable can be determined. On the other hand, the waveform of each state variable obtained from the real system or a nonsimplified model can be estimated using Prony method as a linear sum of damped complex exponentials [32]. The proposed modeling precision for each state variable is validated by comparing the participating eigenvalues and their contribution with the damped complex exponentials calculated by the Prony analysis [33]. In this article, the required input waveforms for Prony analysis are provided from real-time OPAL-RT simulator.

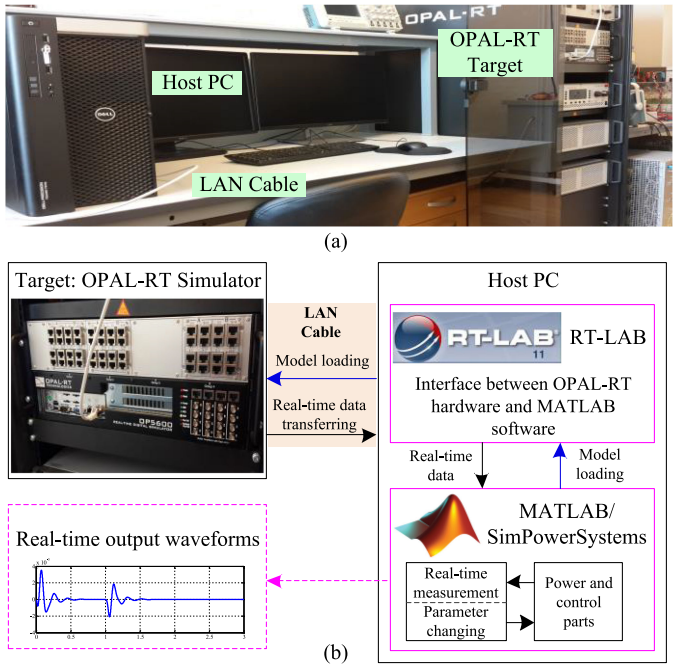

Fig. 9. (a) Real-time experimental setup including the OPAL-RT target, the host PC, and a LAN cable for networking. (b) Real-time simulation process using OPAL-RT digital simulator.

A. OPAL-RT Simulator

In order to indicate the practicality of real-time simulation for large-scale systems, e.g., BTBC-IMGs, real-time software-in-the-loop simulations are provided using OPAL-RT simulator. Fig. 9(a) shows the experimental setup located at Marine Microgrid Laboratory, Aalborg University, including OPAL-RT simulator OP5600 as the target, the host PC, and a networking LAN cable. The OP5600 is configured with four activated Intel Xeon E5, 3.2 GHz processing cores, and works under Linux operating system. Moreover, it provides user-programmable I/O management, handled by a fast Xilinx Spartan-3 FPGA. The real-time simulation process is shown in Fig. 9(b). Version 11.2.1.91 of RT-LAB software is used as the interface between MATLAB and OPAL-RT digital simulator.

In order to simulate BTBC-IMGs as real time, the MATLAB/SimPowerSystems model is loaded on the OPAL-RT via the RT-LAB, then, the real-time data comes back to

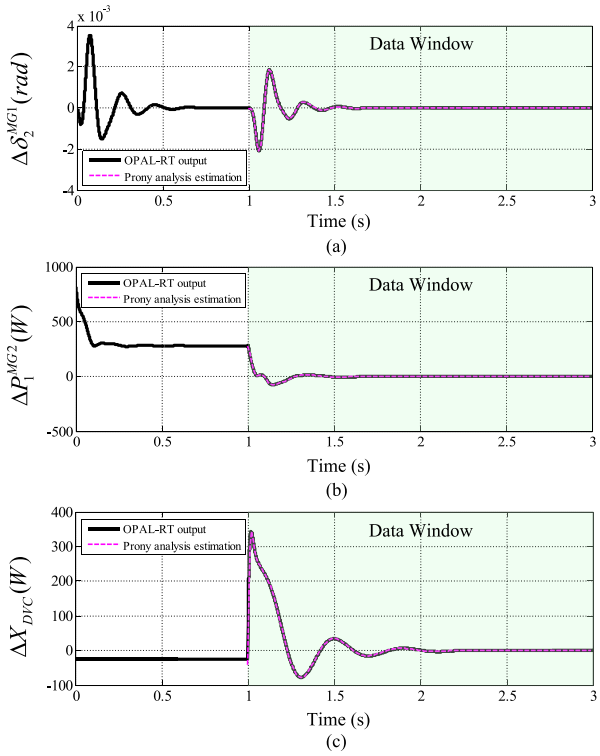

Fig. 10. Prony analysis-based estimation for perturbed form of OPAL-RT output waveforms: (a) seven angle difference of the DER_2 reference frame from the common reference frame of MG_1; (b) DER_1 active power of MG_2; and (c) integrator output of the dc voltage controller.

the MATLAB environment inversely. The SimPowerSystems model should be divided into two subsystems, i.e., a subsystem comprising all permanent power and control parts during the real-time simulation and a subsystem including displays and changeable parameters. After model loading and real-time data reception, real-time waveforms can be measured in SimPowerSystems environment.

B. Interconnection Method Validation Using Prony Analysis

The introduced Prony analysis-based validation method is used for BTBC-IMGs. The details are not given here due to lack of space. The two BTBC-IMGs introduced in [37, Part II] is simulated real time using OPAL-RT simulator. The waveforms of OPAL-RT output and Prony analysis estimation are shown in Fig. 10 for $\Delta\delta_2^{MG1}$, ΔP_1^{MG2}, and $\Delta X_{\rm DVC}$, where generally $\Delta x = x_{\rm ref} - x$, Δx is the perturbed form of the state variable (x) and $x_{\rm ref}$ is the reference value. The Prony method estimates the perturbed form of waveforms for a certain set point, which is 850 W active power flow from MG_2 to MG_1 at $t = 1$ s due to a power deficiency in MG_1. The data window shows the time interval of Prony estimation. All three waveforms show appropriate estimation by Prony analysis.

Comparative results for the estimated state variables are shown in Table II, where the eigenvalues and participation factors are also calculated for the two BTBC-IMGs. The model validation error (MVE) indicates the difference between estimated modes (by Prony analysis) and calculated eigenvalues (by

TABLE II
PRONY ANALYSIS-BASED MODEL VALIDATION

State variable	Eigenvalue	MVE (%)	Participation factor	MVE (%)
$\Delta\delta_2^{MG1}$	$-8 \pm j28.8$	5	0.96	8
	$-145 \pm j106$	8	0.03	3
ΔP_1^{MG2}	$-8 \pm j28.8$	3	0.66	6
	-21.46	7	0.02	21
	-20	0	0.29	9
ΔX_{DVC}	$-2 \pm j13.8$	6	0.45	3
	$-108 \pm j87$	8	0.55	3

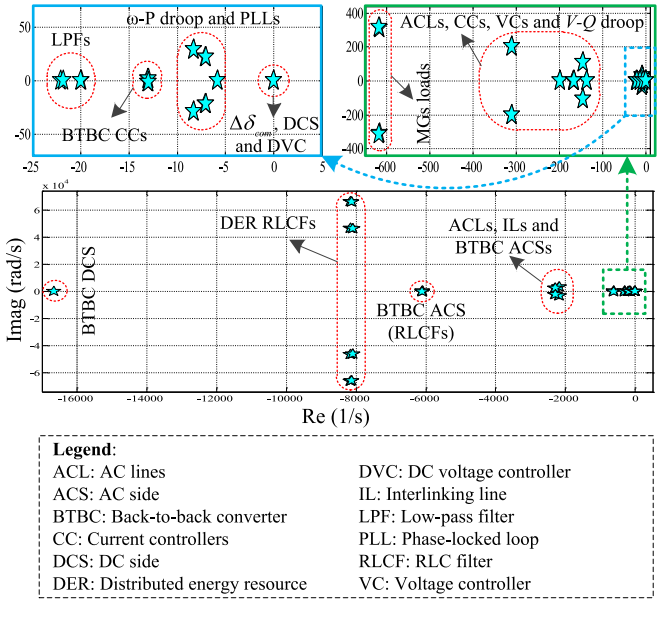

Fig. 11. All eigenvalues of the two interconnected microgrids.

eigenvalue analysis) in the third column, and it shows the difference between normalized estimated amplitudes of the modes and participation factors (calculated by participation matrix) in the fifth column. In the first case, the MVE is calculated as relative error percentage

$$\text{MVE} = \frac{|\gamma - \lambda|}{|\lambda|} \times 100 \tag{30}$$

where γ is a complex conjugate/real mode estimated by Prony analysis and λ is the correlated eigenvalue calculated via eigenvalue analysis. In the second case, the MVE is also calculated through (30), while γ is the normalized estimated amplitude and λ is the correlated participation factor.

The MVE is less than 10% in all cases except $\lambda = -21.46$, which is not an effective dominant mode based on its participation factor, i.e., 0.02. The presented Prony-based validation is able to be employed for all state variables.

V. EIGENVALUE ANALYSIS RESULTS

As mentioned, the required information for simulation is presented in [37, Part II]. Fig. 11 shows all eigenvalues of the two IMGs through one BTBC, where the corresponding modules to each eigenvalue cluster are indicated generally using the participation matrix. The eigenvalues around -5000 real to

-8000 real are mostly affected by DER and BTBC *RLC* filters. The eigenvalues between -2000 real and -3000 real are due to the ac lines, ILs, and BTBC ac sides. More dominant modes can be categorized into three clusters. The cluster near to -600 real is due to the MG loads. The eigenvalue cluster between -100 real and -350 real generally indicates the dynamic participation of the ac lines, DER current controllers, DER voltage controllers, and $V-Q$ droop characteristics. The dominant critical modes (third cluster) are related to the LPFs, BTBC current controllers, BTBC PLLs, $\omega-P$ droop characteristics, dc side, dc voltage controller, and $\Delta\delta_{\text{com}}$, which show the considerable impact of BTBC on the IMG stability.

VI. Conclusion

This article has investigated the small-signal modeling of fully power-electronics-based interconnected autonomous ac microgrids comprising VSC-based DERs and BTBCs exchanging power. For this purpose, the detailed module models are obtained, and their interconnections are realized employing convenient functions of robust control toolbox in MATLAB. The presented small-signal model is comprehensive and can be easily generalized for each number of autonomous ac MGs due to the expandability feature of the proposed interconnection method. It is validated using a Prony method and real-time simulation results, where the state variables are compared with their waveforms simulated in OPAL-RT simulator. Although, the validation is presented only for three state variables, each state variable within the model can be validated in the same way. The most effective state variables/modules on the critical modes show a remarkable effect of BTBCs on the stability of interconnected autonomous microgrids. More conclusions are given in Part II of this article based on sensitivity analysis and time-domain simulations.

References

[1] H. Bevrani, B. François, and T. Ise, *Microgrid Dynamics and Control*. Hoboken, NJ, USA: Wiley, 2017.

[2] C. Chen, J. Wang, F. Qiu, and D. Zhao, "Resilient distribution system by microgrids formation after natural disasters," *IEEE Trans. Smart Grid*, vol. 7, no. 2, pp. 958–966, Mar. 2016.

[3] M. Shahidehpour, Z. Li, S. Bahramirad, Z. Li, and W. Tian, "Networked microgrids: Exploring the possibilities of the IIT-Bronzeville grid," *IEEE Power Energy Mag.*, vol. 15, no. 4, pp. 63–71, Jul./Aug. 2017.

[4] E. Bullich-Massagué *et al.*, "Microgrid clustering architectures," *Appl. Energy*, vol. 212, pp. 340–361, 2018.

[5] S. Moayedi and A. Davoudi, "Distributed tertiary control of dc microgrid clusters," *IEEE Trans. Power Electron.*, vol. 31, no. 2, pp. 1717–1733, Feb. 2016.

[6] Q. Shafiee, T. Dragičević, J. C. Vasquez, and J. M. Guerrero, "Hierarchical control for multiple dc-microgrids clusters," *IEEE Trans. Energy Convers.*, vol. 29, no. 4, pp. 922–933, Dec. 2014.

[7] E. Pashajavid, A. Ghosh, and F. Zare, "A multimode supervisory control scheme for coupling remote droop-regulated microgrids," *IEEE Trans. Smart Grid*, vol. 9, no. 5, pp. 5381–5392, Sep. 2018.

[8] L. Che, M. Shahidehpour, A. Alabdulwahab, and Y. Al-Turki, "Hierarchical coordination of a community microgrid with ac and dc microgrids," *IEEE Trans. Smart Grid*, vol. 6, no. 6, pp. 3042–3051, Nov. 2015.

[9] M. J. Hossain, M. A. Mahmud, F. Milano, S. Bacha, and A. Hably, "Design of robust distributed control for interconnected microgrids," *IEEE Trans. Smart Grid*, vol. 7, no. 6, pp. 2724–2735, Nov. 2016.

[10] I. P. Nikolakakos, H. H. Zeineldin, M. S. El-Moursi, and N. D. Hatziargyriou, "Stability evaluation of interconnected multi-inverter microgrids through critical clusters," *IEEE Trans. Power Syst.*, vol. 31, no. 4, pp. 3060–3072, Jul. 2016.

[11] R. Zamora and A. K. Srivastava, "Multi-layer architecture for voltage and frequency control in networked microgrids," *IEEE Trans. Smart Grid*, vol. 9, no. 3, pp. 2076–2085, May 2018.

[12] M. S. Golsorkhi, D. J. Hill, and H. R. Karshenas, "Distributed voltage control and power management of networked microgrids," *IEEE J. Emerg. Sel. Topics Power Electron.*, vol. 6, no. 4, pp. 1892–1902, Dec. 2018.

[13] P. C. Loh, D. Li, Y. K. Chai, and F. Blaabjerg, "Autonomous operation of hybrid microgrid with ac and dc subgrids," *IEEE Trans. Power Electron.*, vol. 28, no. 5, pp. 2214–2223, May 2013.

[14] X. Wu *et al.*, "A two-layer distributed control method for islanded networked microgrid systems," *IEEE Trans. Smart Grid*, to be published, 2019, doi: 10.1109/TSG.2019.2928330.

[15] Z. Zhao, P. Yang, Y. Wang, Z. Xu, and J. M. Guerrero, "Dynamic characteristics analysis and stabilization of PV-based multiple microgrid clusters," *IEEE Trans. Smart Grid*, vol. 10, no. 1, pp. 805–818, 2019.

[16] F. Shahnia and A. Arefi, "Eigen analysis-based small signal stability of the system of coupled sustainable microgrids," *Int. J. Elect. Power Energy Syst.*, vol. 91, pp. 42–60, 2017.

[17] H.-J. Yoo, T.-T. Nguyen, and H.-M. Kim, "Multi-frequency control in a stand-alone multi-microgrid system using a back-to-back converter," *Energies*, vol. 10, no. 6, pp. 1–18, 2017.

[18] I. U. Nutkani, P. C. Loh, and F. Blaabjerg, "Distributed operation of interlinked ac microgrids with dynamic active and reactive power tuning," *IEEE Trans. Ind. Appl.*, vol. 49, no. 5, pp. 2188–2196, Sep./Oct. 2013.

[19] C.-Y. Tang, Y.-F. Chen, Y.-M. Chen, and Y.-R. Chang, "DC-link voltage control strategy for three-phase back-to-back active power conditioners," *IEEE Trans. Ind. Electron.*, vol. 62, no. 10, pp. 6306–6316, Oct. 2015.

[20] J. Suh, D.-H. Yoon, Y.-S. Cho, and G. Jang, "Flexible frequency operation strategy of power system with high renewable penetration," *IEEE Trans. Sustain. Energy*, vol. 8, no. 1, pp. 192–199, Jan. 2017.

[21] R. Majumder and G. Bag, "Parallel operation of converter interfaced multiple microgrids," *Int. J. Elect. Power Energy Syst.*, vol. 55, pp. 486–496, 2014.

[22] R. Majumder, A. Ghosh, G. Ledwich, and F. Zare, "Power management and power flow control with back-to-back converters in a utility connected microgrid," *IEEE Trans. Power Syst.*, vol. 25, no. 2, pp. 821–834, May 2010.

[23] N. Pogaku, M. Prodanovic, and T. C. Green, "Modeling, analysis, and testing of autonomous operation of an inverter-based microgrid," *IEEE Trans. Power Electron.*, vol. 22, no. 2, pp. 613–625, Mar. 2007.

[24] N. Bottrell, M. Prodanovic, and T. C. Green, "Dynamic stability of a microgrid with an active load," *IEEE Trans. Power Electron.*, vol. 28, no. 11, pp. 5107–5119, Nov. 2013.

[25] A. Kahrobaeian and Y. A.-R. I. Mohamed, "Analysis and mitigation of low-frequency instabilities in autonomous medium-voltage converter-based microgrids with dynamic loads," *IEEE Trans. Ind. Electron.*, vol. 61, no. 4, pp. 1643–1658, Apr. 2014.

[26] I. P. Nikolakakos, H. Zeineldin, M. S. El-Moursi, and J. L. Kirtley, "Reduced-order model for inter-inverter oscillations in islanded droop-controlled microgrids," *IEEE Trans. Smart Grid*, vol. 9, no. 5, pp. 4953–4963, Sep. 2018.

[27] M. Naderi, Y. Khayat, Q. Shafiee, H. Bevrani, and F. Blaabjerg, "Modeling of islanded microgrids using static and dynamic equivalent Thevenin circuits," in *Proc. 20th IEEE Eur. Conf. Power Electron. Appl.*, 2018, pp. 1–10.

[28] Y. Khayat *et al.*, "Decentralized optimal frequency control in autonomous microgrids," *IEEE Trans. Power Syst.*, vol. 34, no. 3, pp. 2345–2353, May 2019.

[29] Z. Shuai, Y. Peng, X. Liu, Z. Li, J. M. Guerrero, and Z. J. Shen, "Dynamic equivalent modeling for multi-microgrid based on structure preservation method," *IEEE Trans. Smart Grid*, vol. 10, no. 4, pp. 3929–3942, Jul. 2019.

[30] F. Shahnia, "Stability and eigen analysis of a sustainable remote area microgrid with a transforming structure," *Sustain. Energy, Grids Netw.*, vol. 8, pp. 37–50, 2016.

[31] Y. Zhang, L. Xie, and Q. Ding, "Interactive control of coupled microgrids for guaranteed system-wide small signal stability," *IEEE Trans. Smart Grid*, vol. 7, no. 2, pp. 1088–1096, Mar. 2016.

[32] S. Jiang, U. Annakkage, and A. Gole, "A platform for validation of facts models," *IEEE Trans. Power Del.*, vol. 21, no. 1, pp. 484–491, Jan. 2006.

[33] H. Golpîra, M. R. Haghifam, and H. Seifi, "Dynamic power system equivalence considering distributed energy resources using Prony analysis," *Int. Trans. Elect. Energy Syst.*, vol. 25, no. 8, pp. 1539–1551, 2015.

[34] Q. Shafiee, J. M. Guerrero, and J. C. Vasquez, "Distributed secondary control for islanded microgrids—A novel approach," *IEEE Trans. Power Electron.*, vol. 29, no. 2, pp. 1018–1031, Feb. 2014.

[35] G. J. Balas, J. C. Doyle, K. Glover, A. Packard, and R. Smith, *μ-Analysis and Synthesis Toolbox: For Use With Matlab*. Natick, MA, USA: MathWorks, 1994.
[36] A. Yazdani and R. Iravani, *Voltage-Sourced Converters in Power Systems*, vol. 34. Piscataway, NJ, USA: Wiley-IEEE Press, 2010.
[37] M. Naderi, Y. Khayat, Q. Shafiee, T. Dragicevic, H. Bevrani, and F. Blaabjerg, "Interconnected autonomous ac microgrids via back-to-back converters—Part II: Stability analysis," submitted for publication.

Mobin Naderi (S'16) was born in Paveh, Iran. He received the B.Sc. and M.Sc. degrees in electrical engineering from Tabriz University, Tabriz, Iran, in 2012, and Iran University of Science and Technology, Tehran, Iran, in 2014, respectively. He was a Visiting Ph.D. Student with the Department of Energy Technology, Aalborg University, Aalborg, Denmark. He is currently working toward the Ph.D. degree in the control of power systems with the University of Kurdistan, Kurdistan, Iran.

His research interests focus on robust control methods, and modeling and the stability and control of autonomous and interconnected ac microgrids.

Yousef Khayat (S'16) received the B.Sc. degree from Urmia University, Urmia, Iran, and the M.Sc. degree (with Hons.) from the Iran University of Science and Technology (IUST), Tehran, Iran, both in electrical engineering, in 2012 and 2014, respectively. He is currently working toward the Ph.D. degree in the control of power systems with the University of Kurdistan, Kurdistan, Iran. He is also a Visiting Ph.D. Student with Aalborg University, Aalborg, Denmark.

His research interests include microgrid dynamics and control and robust, predictive, and nonlinear control for application of power electronics in distributed systems.

Qobad Shafiee (S'13–M'15–SM'17) received the Ph.D. degree in electrical engineering Aalborg University, Aalborg, Denmark, in 2014.

He is currently an Assistant Professor, Associate Director of International Relations, and the Program Co-Leader of the Smart/Micro Grids Research Center, University of Kurdistan, Sanandaj, Iran, where he was a Lecturer from 2007 to 2011. In 2014, he was a Visiting Scholar with the Electrical Engineering Department, the University of Texas at Arlington, Arlington, TX, USA. He was a Postdoctoral Fellow with the Department of Energy Technology, Aalborg University in 2015. His current research interests include modeling, energy management, control of power electronics-based systems and microgrids, and model predictive and optimal control of modern power systems.

Tomislav Dragičević (S'09–M'13–SM'17) received the M.Sc. and the Industrial Ph.D. degrees in electrical engineering from the Faculty of Electrical Engineering, Zagreb, Croatia, in 2009 and 2013, respectively.

From 2013 to 2016, he was a Postdoctoral Research Associate with Aalborg University, Aalborg, Denmark. Since March 2016, he has been an Associate Professor with Aalborg University, where he leads an Advanced Control Lab. He has been a Guest Professor with Nottingham University, U.K., during the spring/summer of 2018. He has authored and coauthored more than 180 technical papers (more than 80 of them are in international journals, mostly IEEE TRANSACTIONS) in his domain of interest, eight book chapters, and a book in the field. His main research interest is the design and control of microgrids, and the application of advanced modeling and control concepts to power electronic systems.

Dr. Dragičević was a recipient of the Konar Prize for the Best Industrial Ph.D. Thesis in Croatia, and a Robert Mayer Energy Conservation Award. He is the Associate Editor for the IEEE TRANSACTIONS ON INDUSTRIAL ELECTRONICS, IEEE JOURNAL OF EMERGING AND SELECTED TOPICS IN POWER ELECTRONICS, and the IEEE INDUSTRIAL ELECTRONICS MAGAZINE.

Hassan Bevrani (S'90–M'04–SM'08) received the Ph.D. degree in electrical engineering from Osaka University, Osaka, Japan, in 2004.

He is currently a Full Professor and the Program Leader of Smart/Micro Grids Research Center (SMGRC) at the University of Kurdistan (UOK). From 2016 to 2019, he was the UOK Vice-Chancellor for Research and Technology. Over the years, he has worked as a Senior Research Fellow and Visiting Professor with Osaka University, Kumamoto University (Japan), Queensland University of Technology (Australia), Kyushu Institute of Technology (Japan), Centrale Lille (France), and the Technical University of Berlin (Germany). He has authored six international books, 15 book chapters, and more than 300 journals/conference papers. His current research interests include smart grid operation and control, power systems stability and optimization, microgrid dynamics and control, and intelligent/robust control applications in power electric industry.

Frede Blaabjerg (S'86–M'88–SM'97–F'03) received the Ph.D. degree in electrical engineering from Aalborg University, Aalborg, Denmark, in 1995.

From 1987 to 1988, he was with ABB-Scandia, Randers, Denmark. He became an Assistant Professor in 1992, an Associate Professor in 1996, and a Full Professor of power electronics and drives in 1998. In 2017, he became a Villum Investigator. He is *honoris causa* with University Politehnica Timisoara (UPT), Romania and Tallinn Technical University (TTU), Estonia. He has authored or coauthored more than 600 journal papers in the fields of power electronics and its applications. He is the co-author of four monographs and the editor of ten books in power electronics and its applications. His current research interests include power electronics and its applications such as in wind turbines, PV systems, reliability, harmonics, and adjustable speed drives.

Prof. Blaabjerg was the recipient of 30 IEEE Prize Paper Awards, the IEEE PELS Distinguished Service Award in 2009, the EPE-PEMC Council Award in 2010, the IEEE William E. Newell Power Electronics Award 2014, and the Villum Kann Rasmussen Research Award 2014. He was the Editor-in-Chief of the IEEE TRANSACTIONS ON POWER ELECTRONICS from 2006 to 2012. He has been a Distinguished Lecturer for the IEEE Power Electronics Society from 2005 to 2007 and for the IEEE Industry Applications Society from 2010 to 2011 as well as from 2017 to 2018. During 2019–2020, he is the President of the IEEE Power Electronics Society. He is the Vice-President of the Danish Academy of Technical Sciences as well. He was nominated in 2014–2018 by Thomson Reuters to be one of the 250 most cited researchers in engineering, around the world.